1   **Utsu aftershock productivity law explained from geometric operations on the**

2   **permanent static stress field of mainshocks**   1

3   Arnaud Mignan*

5   Institute of Geophysics, Swiss Federal Institute of Technology, Zurich

6   *Address:* ETHZ, Institute of Geophysics, NO H66, Sonneggstrasse 5, CH-8092 Zurich

8   *Correspondence to:* arnaud.mignan@sed.ethz.ch

Abstract: The aftershock productivity law is an exponential function of the form $K \propto \exp(\alpha M)$ with K the number of aftershocks triggered by a given mainshock of magnitude M and $\alpha \approx \ln(10)$ the productivity parameter. This law remains empirical in nature although it has also been retrieved in static stress simulations. Here, we explain this law based on the Solid Seismicity Postulate (SSP), the basis of a geometrical theory of seismicity where seismicity patterns are described by mathematical expressions obtained from geometric operations on a permanent static stress field. We first test the SSP that relates seismicity density to a static stress step function. We show that it yields a power exponent $q = 1.96 \pm 0.01$ for the power-law spatial linear density distribution of aftershocks, once uniform noise is added to the static stress field, in agreement with observations. We then recover the exponential function of the productivity law with a break in scaling obtained between small and large M, with $\alpha = 1.5\ln(10)$ and $\ln(10)$, respectively, in agreement with results from previous static stress simulations. Possible biases of aftershock selection, verified to exist in Epidemic-Type Aftershock Sequence (ETAS) simulations, may explain the lack of break in scaling observed in seismicity catalogues. The existence of the theoretical kink remains however to be proven. Finally, we describe how to estimate the Solid Seismicity parameters (activation density δ_+, aftershock solid envelope r_* and background stress amplitude range Δo_*) for large M values.

1. Introduction

Aftershocks, one of the most studied patterns observed in seismicity, are characterized by three empirical laws, which are functions of time, such as the Modified Omori law (e.g., Utsu et al., 1995), space (e.g., Richards-Dinger et al., 2010; Moradpour et al., 2014), and mainshock magnitude (Utsu, 1970a; b; Ogata, 1988).

35 The present study focuses on the latter relationship, i.e., the Utsu aftershock

36 productivity law, which describes the total number of aftershocks K produced by a

37 mainshock of magnitude M as

38 $$K(M) = K_0\exp[\alpha(M - m_0)] \tag{1}$$

39 with m_0 the minimum magnitude cutoff (Utsu, 1970b; Ogata, 1988). This relationship

40 was originally proposed by Utsu (1970a; b) by combining two other empirical laws,

41 the Gutenberg-Richter relationship (Gutenberg and Richter, 1944) and Båth's law

42 (Båth, 1964), respectively:

43 $$\begin{cases} N(\geq m) = A\exp[-\beta(m - m_0)] \\ \quad N(\geq M - \Delta m_B) = 1 \end{cases} \tag{2}$$

44 with N the number of events above magnitude m, A a seismic activity constant, β the

45 magnitude size ratio (or $b = \beta/\ln(10)$ in base-10 logarithmic scale) and Δm_B the

46 magnitude difference between the mainshock and its largest aftershock, such that

47 $$K(M) = N(\geq m_0|M) = \exp(-\beta\Delta m_B)\exp[\beta(M - m_0)] \tag{3}$$

48 with $K_0 = \exp(-\beta\Delta m_B)$ and $\alpha \equiv \beta$. Eq. (3) was only implicit in Utsu (1970a) and

49 not exploited in Utsu (1970b) where K_0 was fitted independently of the value taken by

50 Båth's parameter Δm_B. The α-value was in turn decoupled from the β–value in later

51 studies (e.g., Seif et al. (2017) and references therein).

52   Although it seems obvious that Eq. (1) can be explained geometrically if the

53 volume of the aftershock zone is correlated to the mainshock surface area S with

54 $$S(M) = 10^{M-4} = \exp[\ln(10)(M - 4)] \tag{4}$$

55 (Kanamori and Anderson, 1975; Yamanaka and Shimazaki, 1990; Helmstetter, 2003),

56 there is so far no analytical, physical expression of Eq. (1) available. Although Hainzl

57 et al. (2010) retrieved the exponential behavior in numerical simulations where

58 aftershocks were produced by the permanent static stress field of mainshocks of

59   different magnitudes, it remains unclear how K_0 and α relate to the underlying

60   physical parameters.

61   The aim of the present article is to explain the Utsu aftershock productivity

62   equation (Eq. 1) by applying a geometrical theory of seismicity (based on the Solid

63   Seismicity Postulate, SSP), which has already been shown to effectively explain other

64   empirical laws of both natural and induced seismicity from simple geometric

65   operations on a permanent static stress field (Mignan, 2012; 2016a). The theory is

66   applied here for the first time to the case of aftershocks.

67

68   **2. Physical Expression of the Aftershock Productivity Law**

69   *2.1. Demonstration of the productivity law by geometric operations*

70   "Solid Seismicity", a geometrical theory of seismicity, is based on the

71   following Postulate (Mignan et al., 2007; Mignan, 2008, 2012; 2016a):

72

73   **Solid Seismicity Postulate (SSP):** *Seismicity can be strictly categorized*

74   *into three regimes of constant spatiotemporal densities δ – background*

75   *δ_0, quiescence δ_- and activation δ_+ (with $\delta_- \ll \delta_0 \ll \delta_+$) - occurring*

76   *respective to the static stress step function:*

77
$$\delta(\sigma) = \begin{cases} \delta_- & , \sigma < -\Delta o_* \\ \delta_0 & , \sigma \le |\pm\Delta o_*| \\ \delta_+ & , \sigma > \Delta o_* \end{cases} \qquad (5)$$

78   *with σ the static stress [bar], Δo_* the background stress amplitude range*

79   *[bar], a stress threshold value separating two seismicity regimes, and δ*

80   *the spatial density of events [events/km^3] per regime.*

81

82   We mean by "strictly categorized" that any seismicity population is either part of the

83   background, quiescence or activation regime (or class), with no other regime/class

84   possible (i.e., a sort of hard labelling). Based on this Postulate, Mignan (2012)

85   demonstrated the power-law behavior of precursory seismicity in agreement with the

86   observed time-to-failure equation (Varnes, 1989), while Mignan (2016a)

87   demonstrated both the observed parabolic spatiotemporal front and the linear

88   relationship with injection-flow-rate of induced seismicity (Shapiro and Dinske,

89   2009). It remains unclear whether the SSP has a physical origin or not. If not, it would

90   still represent a reasonable approximation of the linear relationship between event

91   production and static stress field in a simple clock-change model (Hainzl et al., 2010;

92   Fig. 1a). For the testing of the SSP on the observed spatial distribution of aftershocks,

93   see section 2.2. The power of Eq. (5) is that it allows defining seismicity patterns in

94   terms of "solids" described by the spatial envelope $r_* = r(\sigma = \pm \Delta o_*)$ where r is the

95   distance from the static stress source (e.g., mainshock rupture) and r_* the distance r at

96   which there is a change of regime (quiescence/background at $\sigma = -\Delta o_*$ or

97   background/activation at $\sigma = \Delta o_*$). The spatiotemporal rate of seismicity is then a

98   mathematical expression defined by the density of events δ times the volume

99   characterized by r_* (see previous demonstrations in Mignan et al. (2007) and Mignan

100   (2011; 2012; 2016a) where simple algebraic expressions were obtained).

101   In the case of aftershocks, we define the static stress field of the mainshock by

102   $$\sigma(r) = -\Delta\sigma_0 \left[\left(1 - \frac{c^3}{(r+c)^3}\right)^{-1/2} - 1 \right] \tag{6}$$

103   with $\Delta\sigma_0 < 0$ the mainshock stress drop, c the crack radius and r the distance from the

104   crack. Eq (6) is a simplified representation of stress change from slip on a planar

105   surface in a homogeneous elastic medium. It takes into account both the square root

106   singularity at crack tip and the $1/r^3$ falloff at higher distances (Dieterich, 1994; Fig.

107   1b). It should be noted that this radial static stress field does not represent the

108   geometric complexity of Coulomb stress fields (Fig. 2a). However we are here only

109   interested in the general behavior of aftershocks with Eq. (6) retaining the first-order

110   characteristics of this field (i.e., on-fault seismicity; Fig. 2b), which corresponds to the

111   case where the mainshock relieves most of the regional stresses and aftershocks occur

112   on optimally oriented faults. It is also in agreement with observations, most

113   aftershocks being located on and around the mainshock fault traces in Southern

114   California (Fig. 2c; see section "Observations & Model Fitting"). The occasional

115   cases where aftershocks occur off-fault (e.g., Ross et al., 2017) can be explained by

116   the mainshock not relieving all of the regional stress (King et al., 1994; Fig. 2d).

117   For $r_* = r(\sigma = \Delta o_*)$, Eq. (6) yields the aftershock solid envelope of the form:

118
$$r_*(c) = \left\{ \frac{1}{\left[1 - \left(1 - \frac{\Delta\sigma_*}{\Delta\sigma_0} \right)^{-2} \right]^{1/3}} - 1 \right\} c = Fc, \qquad (7)$$

119   function of the crack radius c and of the ratio between background stress amplitude

120   range Δo_* and stress drop $\Delta\sigma_0$ (Fig. 1c). With $\Delta\sigma_0$ independent of earthquake size

121   (Kanamori and Anderson, 1975; Abercrombie and Leary, 1993) and Δo_* assumed

122   constant, r_* is directly proportional to c with proportionality constant, or stress factor,

123   F (Eq. 7). Geometrical constraints due to the seismogenic layer width w_0 then yield

124
$$c(M) = \begin{cases} \left(\frac{S(M)}{\pi} \right)^{1/2} & , S(M) \leq \pi w_0^2 \\ w_0 & , S(M) > \pi w_0^2 \end{cases} \qquad (8)$$

125   with S the rupture surface area defined by Eq. (4) and c becoming an effective crack

126   radius (Kanamori and Anderson, 1975; Fig. 1d). Note that the factor of 2 (i.e., using

127   w_0 instead of $w_0/2$) comes from the free surface effect (e.g., Kanamori and Anderson,

128   1975; Shaw and Scholz, 2001).

129   The aftershock productivity $K(M)$ is then the activation density δ_+ times the

130   volume $V_*(M)$ of the aftershock solid. For the case in which the mainshock relieves

131   most of the regional stress, stresses are increased all around the rupture (King et al.,

132   1994), which is topologically identical to stresses increasing radially from the rupture

133   plane (Fig. 2a-b). It follows that the aftershock solid can be represented by a volume

134   of contour $r_*(M)$ from the rupture plane geometric primitive, i.e., a disk or a

135   rectangle, for small and large mainshocks, respectively. This is illustrated in Figure

136   3a-b and can be generalized by

137    $$V_*(M) = 2r_*(M)S(M) + \frac{\pi}{2}r_*^2(M)d \qquad (9)$$

138   where d is the distance travelled around the geometric primitive by the geometric

139   centroid of the semi-circle of radius $r_*(M)$ (i.e., Pappus's Centroid Theorem), or

140    $$d = \begin{cases} 2\pi\left(c(M) + \frac{4}{3\pi}r_*(M)\right) & , c(M) + r_*(M) \leq \frac{w_0}{2} \\ 2w_0 & , c(M) + r_*(M) > \frac{w_0}{2} \end{cases} \qquad (10)$$

141   For the disk, the volume (Eq. 9) corresponds to the sum of a cylinder of radius $c(M)$

142   and height $2r_*(M)$ (first term) and of half a torus of major radius $c(M)$ and minus

143   radius $r_*(M)$ (second term). For the rectangle, the volume is the sum of a cuboid of

144   length $l(M)$ (i.e., rupture length), width w_0 and height $2r_*(M)$ (first term) and of a

145   cylinder of radius $r_*(M)$ and height w_0 (second term; see red and orange volumes,

146   respectively, in Figure 3a-c). Finally inserting Eqs. (7), (8) and (10) into (9), we

147   obtain

148    $$K(M) = \delta_+ \begin{cases} \left[\frac{2F}{\sqrt{\pi}} + F^2\sqrt{\pi}\left(1 + \frac{4}{3\pi}F\right)\right]S^{3/2}(M) & , S(M) \leq \left(\frac{w_0\sqrt{\pi}}{2(1+F)}\right)^2 \\ \frac{2F}{\sqrt{\pi}}S^{3/2}(M) + F^2 w_0 S(M) & \left(\frac{w_0\sqrt{\pi}}{2(1+F)}\right)^2 < S(M) \leq \pi w_0^2 \\ 2Fw_0 S(M) + \pi F^2 w_0^3 & , S(M) > \pi w_0^2 \end{cases}$$

149   (11)

150   which is represented in Figure 3d. Considering the two main regimes only (small

151   versus large mainshocks) and inserting Eq. (4) into (11), we get

152    $$K(M) = \delta_+ \begin{cases} \left[\frac{2F}{\sqrt{\pi}} + F^2\sqrt{\pi}\left(1 + \frac{4}{3\pi}F\right)\right]\exp\left[\frac{3\ln(10)}{2}(M-4)\right] & \text{, small } M \\ 2Fw_0\exp[\ln(10)(M-4)] + \pi F^2 w_0^3 & \text{, large } M \end{cases} \quad (12)$$

153   which is a closed-form expression of the same form as the original Utsu productivity

154   law (Eq. 1). Note that K and δ_+ are both, implicitly, function of the selected minimum

155   aftershock magnitude threshold m_0.

156   Here, we predict that the α-value decreases from $3\ln(10)/2 \approx 3.45$ to $\ln(10) \approx$

157   2.30 when switching regime from small to large mainshocks (or from 1.5 to 1 in base-

158   10 logarithmic scale). It should be noted that Hainzl et al. (2010) observed the same

159   break in scaling in static stress transfer simulations, which corroborates our analytical

160   findings. Hainzl et al. (2010) simulated aftershocks using the clock-change model

161   where events were advanced in time by the static stress change produced by a

162   mainshock in a three-dimensional medium. They explained the scaling break

163   observed in simulation as a transition from 3D to 2D scaling regime when the

164   mainshock rupture dimension approached w_0, which is compatible with the present

165   demonstration. For large M, the scaling is fundamentally the same as in Eq. (4). Since

166   that relation also explains the slope of the Gutenberg-Richter law (see physical

167   explanation given by Kanamori and Anderson,1975), it follows that $\alpha \equiv \beta$, which is

168   also in agreement with the original formulation of Utsu (1970a; b; Eq. 3).

169

170   *2.2. Testing of the SSP on the aftershock spatial distribution*

171   The SSP predicts a step-like behavior of the aftershock spatial density for an

172   idealized smooth static stress field (Fig. 4a-b), which is in disagreement with real

173   aftershock observations. A number of studies have shown that the spatial linear

174   density distribution of aftershocks ρ is well represented by a power-law, expressed as

175     $\rho(r) \propto r^{-q}$ (13)

176   with r the distance from the mainshock and q the power-law exponent. This parameter

177   ranges over $1.3 \leq q \leq 2.5$ (Felzer and Brodsky, 2006; Lipiello et al., 2009; Marsan and

178   Lengliné, 2010; Richards-Dinger et al., 2010; Shearer, 2012; Gu et al., 2013;

179   Moradpour et al., 2014; van der Elst and Shaw, 2015). Although Felzer and Brodsky

180   (2004) suggested a dynamic stress origin for aftershocks, their results were later on

181   questioned by Richards-Dinger et al. (2010). Most of the studies cited above suggest

182   that the q-value is explained from a static stress process. As for the examples of

183   aftershocks shown to be dynamically triggered (e.g., Fan and Shearer, 2016), they are

184   too few to alter the aftershock productivity law and too remote to be consistently

185   defined as aftershocks in cluster methods.

186   In a more realistic setting, the static stress field must be heterogeneous (due to

187   the occurrence of previous events and other potential stress perturbations). We

188   therefore simulate the static stress field by adding a uniform random component

189   bounded over $\pm\Delta o_*$ following Mignan (2011) (see also King and Bowman, 2003).

190   Note that any deviation above Δo_* would be flattened to Δo_* over time by temporal

191   diffusion (so-called "historical ghost static stress field" in Mignan, 2016a). Figure 4c

192   shows the resulting stress field and Figure 4d the predicted aftershock spatial density.

193   Adding uniform noise blurs the contour of the aftershock solid, switching the

194   aftershock spatial density from a step function (Fig. 4b) to a power-law (Fig. 4d). We

195   fit Eq. (13) to the simulated data using the Maximum Likelihood Estimation (MLE)

196   method with $r_{min} = r_*$ (Clauset et al., 2009) and find $q = 1.96\pm0.01$, in agreement with

197 the aftershock literature. This result alone is however insufficient to prove the validity

198 of the SSP.

199

200 **3. Observations & Model Fitting**

201 *3.1. Data*

202 We consider the case of Southern California and extract aftershock sequences

203 from the relocated earthquake catalog of Hauksson et al. (2012) defined over the

204 period 1981-2011, using the nearest-neighbor method (Zaliapin et al., 2008; used with

205 its standard parameters originally calibrated for Southern California, considering only

206 the first aftershock generation). Only events with magnitudes greater than $m_0 = 2.0$ are

207 considered (a conservative estimate following results of Tormann et al. (2014);

208 saturation effects immediately after the mainshock are negligible when considering

209 entire aftershock sequences; Helmstetter et al., 2005).

210

211 *3.2. Aftershock spatial density distribution*

212 Figure 5a represents the spatial linear density distribution of aftershocks $\rho(r)$

213 for the four largest strike-slip mainshocks in Southern California: 1987 *M=6.6*

214 Superstition Hills, 1992 *M=7.3* Landers, 1999 *M=7.1* Hector Mine, and 2010 *M=7.2*

215 El Mayor. The distance between mainshock and aftershocks is calculated as

216 $r = \sqrt{(x - x_0)^2 + (y - y_0)^2}$ with (x, y) the aftershock coordinates and (x_0, y_0) the

217 coordinates of the nearest point to the mainshock fault rupture (as depicted in Figure

218 2c). The dashed black lines shown in Figure 5a are visual guides to $q = 1.96$, showing

219 that the SSP is compatible with real aftershock observations.

220 Comparing Figure 5a to Figure 4d suggests that r_* can be roughly estimated

221 from the spatial linear density plot, being the maximum distance r at which the

222   plateau ends, here leading to $r_* \approx 1$ km. This parameter is constant for different large

223   M values since both w_0 and $\Delta\sigma_0$ are constant while $\Delta\sigma_*$ is also *a priori* a constant. We

224   can then estimate the ratio $\Delta\sigma_*/\Delta\sigma_0$ from Eq. (7). However the result is ambiguous

225   due to uncertainties on the width w_0. For $w_0 = \{5, 10, 15\}$ km, we get $\Delta\sigma_*/\Delta\sigma_0 =\{-$

226    $0.54, -1.01, -1.38\}$.

227   As for the plateau value $\rho(r < r_*)$, it provides an estimate of the aftershock

228   activation density δ_+ with

229    $$\delta_+ = \frac{\rho(M, r < r_*)}{\exp[\ln(10)(M-4)]} \qquad (14)$$

230   a volumetric density, i.e. the linear density ρ normalized by the mainshock rupture

231   area (Eq. 4). Due to the fluctuations in $\rho(r < r_*)$, δ_+ will be estimated from the

232   productivity law instead (see section 3.3) and $\rho(r < r_*)$ then estimated from Eq. (14)

233   (horizontal dashed colored lines), as detailed below.

234   It should be noted that we consider only the first-generation aftershocks to

235   avoid ρ heterogeneities from secondary aftershock clusters occurring off-fault. An

236   example of such heterogeneity/anisotropy is illustrated by the Landers-Big Bear case

237   (Fig. 2c; dotted colored curve on Fig. 5a). Those cases are not systematic and

238   therefore not considered in the aftershock productivity law. However they are also

239   due to static stress changes (e.g., King et al., 1994) with the anisotropic effects

240   explainable by Solid Seismicity through the concept of "historical ghost static stress

241   field" (Mignan, 2016a).

242

243   *3.3. Aftershock productivity law*

244   The observed number n of aftershocks of magnitude $m \geq m_0$ produced by a

245   mainshock of magnitude M (for a total of N mainshocks) in Southern California is

246   shown in Figures 5b (for large $M \geq 6$) and 6a (for the full range $M \geq m_0$). We fit Eq.

247   (1) to the data using the MLE method with the log-likelihood function

248      $LL(\theta; X = \{n_i; i = 1, ..., N\}) = \sum_{i=1}^{N}[n_i \ln[K_i(\theta)] - K_i(\theta) - \ln(n_i!)]$ (15)

249   for a Poisson process, representing the stochasticity of the count K of aftershocks

250   produced by a mainshock at any given time. Inserting Eq. (1) in Eq. (15) yields

251      $LL(\theta = \{K_0, \alpha\}; X) = \ln(K_0) \sum_{i=1}^{N} n_i + \alpha \sum_{i=1}^{N}[n_i(M_i - m_0)] - K_0 \sum_{i=1}^{N} \exp[\alpha(M_i -$

252      $m_0)] - \sum_{i=1}^{N} \ln(n_i!)$ (16)

253   (note that the last term can be set to 0 during LL maximization). For Southern

254   California, we obtain $\alpha_{MLE} = 2.32$ (1.01 in $\log_{10}$ scale) and $K_0 = 0.025$ when

255   considering large $M \geq 6$ mainshocks only to avoid the issues of scaling break and data

256   dispersion at lower magnitudes. This result, represented by the black solid line on

257   Figure 5b, is in agreement with previous studies in the same region (e.g., Helmstetter,

258   2003; Helmstetter et al., 2005; Zaliapin and Ben-Zion, 2013; Seif et al., 2017) and

259   with $\alpha = \ln(10) \approx 2.30$ predicted for large mainshocks in Solid Seismicity (Eq. 12).

260   Moreover we find a bulk $\beta_{MLE} = 2.34$ (1.02 in $\log_{10}$ scale) (Aki, 1965), in agreement

261   with $\alpha \equiv \beta$.

262   Let us now rewrite the Solid Seismicity aftershock productivity law (Eq. 12)

263   by only considering the large M case and injecting $r_* = Fw_0$ (by combining Eqs. 7-8).

264   We get

265      $K(M > M_{break}) = \delta_+\{2r_* \exp[\ln(10)(M - 4)] + \pi r_*^2 w_0\}$ (17)

266   The role of w_0 is illustrated in Figure 5b for different values (dashed and dotted

267   curves) and shown to be insignificant for large M values. Therefore Eq. (17) can be

268   approximated to

269      $K(M > M_{break}) \approx 2\delta_+ r_* \exp[\ln(10)(M - 4)]$ (18)

270   By analogy with Eq. (1), we get

271 $\delta_+ = \frac{K_0 \exp[\ln(10)(4-m_0)]}{2r_*}$ (19)

272 With $r_* \approx 1$ km estimated from $\rho(r)$ (section 3.2) and $K_0 = 0.025$, we obtain $\delta_+ = 1.23$

273 events/km^3 for $m_0 = 2$. We then get back the plateau $\rho(r < r_*)$ for different M values

274 from Eq. (14), as shown in Figure 5a (horizontal dashed colored lines). Although

275 based on limited data, this result suggests that the activation parameter δ_+ is constant

276 (at least for large M) in Southern California. Note that if $\rho(r < r_*)$ was well

277 constrained, it could have been estimated jointly with r_* from Figure 5a to predict the

278 aftershock productivity law of Figure 5b without further fitting required (hence

279 removing K_0 from the equation, K_0 having no physical meaning in Solid Seismicity).

280

281 **4. Role of aftershock selection on productivity scaling-break**

282   We tested the following piecewise model to identify any break in scaling at

283 smaller M, as predicted by Eq. (12):

284 $K(M) = \begin{cases} K_0 \frac{\exp[\ln(10)(M_{break}-m_0)]}{\exp[\frac{3}{2}\ln(10)(M_{break}-m_0)]} \exp\left[\frac{3}{2}\ln(10)(M-m_0)\right] & , M \le M_{break} \\ K_0 \exp[\ln(10)(M-m_0)] & , M > M_{break} \end{cases}$

285   (20)

286 but with the best MLE result obtained for $M_{break} = m_0$, suggesting no break in scaling

287 in the aftershock productivity data, as observed in Figure 6a. Final parameter

288 estimates are $\alpha_{MLE} = 1.95$ (0.85 in $\log_{10}$ scale) and $K_0 = 0.141$ for the full mainshock

289 magnitude range $M \ge m_0$ (dotted line), subject to high scattering at low M values.

290   We now identify whether the lack of break in scaling in aftershock

291 productivity observed in earthquake catalogues could be an artefact related to the

292 aftershock selection method. We run Epidemic-Type Aftershock Sequence (ETAS)

293 simulations (Ogata, 1988; Ogata and Zhuang, 2006), with the seismicity rate

$$
294 \quad
\begin{cases}
\lambda(t, x, y) = \mu(t, x, y) + \sum_{i:t_j<t} K(M_i)f(t - t_i)g(x - x_i, y - y_i|M_i) \\
\qquad\qquad f(t) = c^{p-1}(p - 1)(t + c)^{-p} \\
g(x, y|M) = \frac{1}{\pi}\left(de^{\gamma(M-m_0)}\right)^{q-1}\left(x^2 + y^2 + de^{\gamma(M-m_0)}\right)^{-q}(q - 1)
\end{cases}
\quad (21)
$$

295 Aftershock sequences are defined by power laws, both in time and space (for an

296 alternative temporal function, see Mignan (2015; 2016b); the spatial power-law

297 distribution is in agreement with Solid Seismicity in the case of a heterogeneous static

298 stress field – see section 2.2). μ is the Southern California background seismicity, as

299 defined by the nearest-neighbor method (with same t, x, y and m). We fix the ETAS

300 parameters to $\theta = \{c = 0.011$ day, $p = 1.08$, $d = 0.0019$ km^2, $q = 1.47$, $\gamma = 2.01$, $\beta =$

301 2.29, $K_0 = 0.08\}$, following the fitting results of Seif et al. (2017) for the Southern

302 California relocated catalog and $m_0 = 2$ (see their Table 1). However, we define the

303 productivity function $K(M)$ from Eq. (20) with $M_{break} = 5$. Examples of ETAS

304 simulations are shown in Figure 6b for comparison with the observed Southern

305 California time series. Figure 6c allows us to verify that the simulated aftershock

306 productivity is kinked at M_{break}, as defined by Eq. (20).

307 We then select aftershocks from the ETAS simulations with the nearest-

308 neighbor method. Figure 4d represents the estimated aftershock productivity, which

309 has lost the break in scaling originally implemented in the simulations (with an

310 underestimated $\alpha_{MLE} = 2.07$ as observed in the real case for $M \geq m_0$). Note that a

311 similar result is obtained when using a windowing method (Gardner and Knopoff,

312 1974). This demonstrates that the theoretical break in scaling predicted in the

313 aftershock productivity law can be lost in observations due to an aftershock selection

314 bias, all declustering techniques assuming continuity over the entire magnitude range.

315 While such a bias is possible, it yet does not prove that the break in scaling exists. The

316 fact that a similar break in scaling was obtained in independent Coulomb stress

317 simulations (Hainzl et al., 2010) however provides high confidence in our results.

318   One other possible explanation for lack of scaling break is that our

319   demonstration assumes moment magnitudes while the Southern California catalogue

320   is in local magnitudes. Deichmann (2017) demonstrated that while $M_L \propto M_w$ at large

321   M, $M_L \propto 1.5M_w$ at smaller M values. This could in theory cancel the kink in real data.

322   However the scaling break predicted by Deichmann (2017) occurs at several

323   magnitude units below the geometric scaling break expected by Solid Seismicity,

324   invalidating this second option for mid-range magnitudes M.

325

326   **5. Conclusions**

327   In the present study, a closed-form expression defined from geometric and

328   static stress parameters was proposed (Eq. 12) to explain the empirical Utsu

329   aftershock productivity law (Eq. 1). This demonstration is similar to the previous ones

330   made by the author to explain precursory accelerating seismicity and induced

331   seismicity (Mignan, 2012; 2016b), In all these demonstrations, the main physical

332   parameters remain the same, i.e. the activation density δ_+ (also δ_- and δ_0), the

333   background stress amplitude range Δo_*, and the solid envelope r_* which describes the

334   geometry of the "seismicity solid" (Fig. 3a-b). Further studies will be needed to

335   evaluate whether the δ_+ and Δo_* parameters are universal or region-specific and if the

336   same values apply to different types of seismicity at a same location.

337   Although the Solid Seismicity Postulate (SSP) (Eq. 5) remains to be proven, it

338   is so far a rather convenient and pragmatic assumption to determine the physical

339   parameters that play a first-order role in the behavior of seismicity. The similarity of

340   the SSP-simulated and observed values of the power-law exponent q of the aftershock

341   spatial density distribution shows that the SSP is consistent with large aftershock

342   observations once uniform noise is added to the stress field (Figs. 4d-5a). The impact

343   of other types of noise on q has yet to be investigated. The SSP is also complementary

344   to the more common simulations of static stress loading (King and Bowman, 2003)

345   and static stress triggering (Hainzl et al., 2010).

346   Analytic geometry, providing both a visual representation and an analytical

347   expression of the problem at hand (Fig. 3), represents a new approach to try to better

348   understand the behavior of seismicity. Its current limitation in the case of aftershock

349   analysis consists in assuming that the static stress field is radial and described by Eq.

350   (6) (e.g., Dieterich, 1994), which is likely only valid for mainshocks relieving most of

351   the regional stresses and with aftershocks occurring on optimally oriented faults (King

352   et al., 1994). More complex, second-order, stress behaviors might explain part of the

353   scattering observed around Eq. (1) (Fig. 6a), such as overpressure due to trapped high-

354   pressure gas for example (Miller et al., 2004 – see also Mignan (2016a) for an

355   overpressure field due to fluid injection). Other $\sigma(r)$ formulations could be tested in

356   the future, the only constraint on generating so-called seismicity solids being the use

357   of the postulated static stress step function of Eq. (5) (i.e., the Solid Seismicity

358   Postulate, SSP).

359   Finally, the disappearance of the predicted scaling break in the aftershock

360   productivity law once declustering is applied (Fig. 6) indicates that more work is

361   required in that domain. Only a declustering technique that does not dictate a constant

362   scaling at all M will be able to identify rather a scaling break really exists or not.

363

364   *Acknowledgments:* I thank N. Wetzler and two anonymous reviewers, as well as

365   editor Ilya Zaliapin, for their valuable comments.

366

367   **References**

368 Abercrombie, R. and Leary, P.: Source parameters of small earthquakes recorded at

369   2.5 km depth, Cajon Pass, Southern California: Implications for earthquake

370   scaling, Geophys. Res. Lett., 20, 1511-1514, 1993.

371 Aki, K.: Maximum Likelihood Estimate of b in the Formula log N = a-bM and its

372   Confidence Limits, Bull. Earthq. Res. Instit., 43, 237-239, 1965.

373 Båth, M.: Lateral inhomogeneities of the upper mantle, Tectonophysics, 2, 483-514,

374   1965.

375 Clauset, A., Shalizi, C. R. and Newman, M. E. J.: Power-Law Distributions in

376   Empirical Data, SIAM Review, 51, 661-703, doi: 10.1137/070710111, 2009.

377 Deichmann, N.: Theoretical Basis for the Observed Break in M_L/M_w Scaling between

378   Small and Large Earthquakes, Bull. Seismol. Soc. Am., 107, doi:

379   10.1785/0120160318, 2017.

380 Dieterich, J.: A constitutive law for rate of earthquake production and its application

381   to earthquake clustering, J. Geophys. Res., 99, 2601-2618, 1994.

382 Fan, W. and Shearer, P. M.: Local near instantaneously dynamically triggered

383   aftershocks of large earthquakes, Science, 353, 1133-1136, 2016.

384 Felzer, K. R. and Brodsky, E. E.: Decay of aftershock density with distance indicates

385   triggering by dynamic stress, Nature, 441, 735-738, doi: 10.1038/nature04799,

386   2006.

387 Gardner, J. K. and Knopoff, L.: Is the sequence of earthquakes in Southern California,

388   with aftershocks removed, Poissonian?, Bull. Seismol. Soc. Am., 64, 1363-1367,

389   1974.

390 Gu, C., Schumann, A. Y., Baisesi, M. and Davidsen, J.: Triggering cascades and

391   statistical properties of aftershocks, J. Geophys. Res. Solid Earth, 118, 4278-4295,

392   doi: 10.1002/jgrb.50306, 2013.

393   Gutenberg, B. and Richter, C. F.: Frequency of earthquakes in California, Bull.

394   Seismol. Soc. Am., 34, 185-188, 1944.

395   Hainzl, S., Brietzke, G. B. and Zöller, G.: Quantitative earthquake forecasts resulting

396   from static stress triggering, J. Geophys. Res., 115, B11311, doi:

397   10.1029/2010JB007473, 2010.

398   Hauksson, E., Yang, W. and Shearer, P. M.: Waveform Relocated Earthquake Catalog

399   for Southern California (1981 to June 2011), Bull. Seismol. Soc. Am., 102, 2239-

400   2244, doi: 10.1785/0120120010, 2012.

401   Helmstetter, A.: Is Earthquake Triggering Driven by Small Earthquakes?, Phys. Rev.

402   Lett., 91, doi: 10.1102/PhysRevLett.91.058501, 2003.

403   Helmstetter, A., Kagan, Y. Y. and Jackson, D. D. : Importance of small earthquakes

404   for stress transfers and earthquake triggering, J. Geophys. Res., 110, B05S08, doi:

405   10.1029/2004JB003286, 2005.

406   Kanamori, H. and Anderson, D. L.: Theoretical basis of some empirical relations in

407   seismology, Bull. Seismol. Soc. Am., 65, 1073-1095, 1975.

408   King, G. C. P., Stein, R. S. and Lin, J.: Static Stress Changes and the Triggering of

409   Earthquakes, Bull. Seismol. Soc. Am., 84, 935-953, 1994.

410   King, G. C. P. and Bowman, D. D.: The evolution of regional seismicity between

411   large earthquakes, J. Geophys. Res., 108, 2096, doi: 10.1029/2001JB000783, 2003.

412   Lin, J. and Stein, R. S.: Stress triggering in thrust and subduction earthquakes, and

413   stress interaction between the southern San Andreas and nearby thrust and strike-

414   slip faults, J. Geophys. Res., 109, B02303, doi: 10.1029/2003JB002607, 2004.

415   Lippiello, E., de Arcangelis, J. and Godano, C.: Role of Static Stress Diffusion in the

416   Spatiotemporal Organization of Aftershocks, Phys. Rev. Lett., 103, 038501, doi:

417   10.1103/PhysRevLett.103.038501, 2009.

418   Marsan, D. and Lengliné, O.: A new estimation of the decay of aftershock density

419   with distance to the mainshock, J. Geophys. Res., 115, B09302, doi:

420   10.1029/2009JB007119, 2010.

421   Miller, S. A., Collettini, C., Chiaraluce, L., Cocco, M., Barchi, M. and Kaus, B. J. P.:

422   Aftershocks driven by a high-pressure CO_2 source at depth, Nature, 427, 724-727

423   Mignan, A., King, G. C. P. and Bowman, D.: A mathematical formulation of

424   accelerating moment release based on the stress accumulation model, J. Geophys.

425   Res., 112, B07308, doi: 10.1029/2006JB004671, 2007.

426   Mignan, A.: Non-Critical Precursory Accelerating Seismicity Theory (NC PAST) and

427   limits of the power-law fit methodology, Tectonophysics, 452, 42-50, doi:

428   10.1016/j.tecto.2008.02.010, 2008.

429   Mignan, A.: Retrospective on the Accelerating Seismic Release (ASR) hypothesis:

430   Controversy and new horizons, Tectonophysics, 505, 1-16, doi:

431   10.1016/j.tecto.2011.03.010, 2011.

432   Mignan, A.: Seismicity precursors to large earthquakes unified in a stress

433   accumulation framework, Geophys. Res. Lett., 39, L21308, doi:

434   10.1029/2012GL053946, 2012.

435   Mignan, A.: Modeling aftershocks as a stretched exponential relaxation, Geophys.

436   Res. Lett., 42, 9726-9732, doi: 10.1002/2015GL066232, 2015.

437   Mignan, A.: Static behaviour of induced seismicity, Nonlin. Processes Geophys., 23,

438   107-113, doi: 10.5194/npg-23-107-2016, 2016a.

439   Mignan, A.: Reply to "Comment on 'Revisiting the 1894 Omori Aftershock Dataset

440   with the Stretched Exponential Function' by A. Mignan" by S. Hainzl and A.

441   Christophersen, Seismol. Res. Lett., 87, 1134-1137, doi: 10.1785/0220160110,

442   2016b.

443   Moradpour, J., Hainzl, S. and Davidsen, J.: Nontrivial decay of aftershock density

444   with distance in Souther California, J. Geophys. Res. Solid Earth, 119, 5518-5535,

445   doi: 10.1002/2014JB010940, 2014.

446   Ogata, Y.: Statistical Models for Earthquake Occurrences and Residual Analysis for

447   Point Processes, J. Am. Stat. Assoc., 83, 9-27, 1988.

448   Ogata, Y. and Zhuang, J.: Space-time ETAS models and an improved extension,

449   Tectonophysics, 413, 13-23, doi: 10.1016/j.tecto.2005.10.016, 2006.

450   Richards-Dinger, K., Stein, R. S. and Toda, S.: Decay of aftershock density with

451   distance does not indicate triggering by dynamic stress, Nature, 467, 583-586, doi:

452   10.1038/nature09402, 2010.

453   Ross, Z. E., Hauksson, E. and Ben-Zion, Y.: Abundant off-fault seismicity and

454   orthogonal structures in the San Jacinto fault zone, Sci. Adv., 3, doi:

455   10.1126/sciadv.1601946, 2017.

456   Seif, S., Mignan, A., Zechar, J. D., Werner, M. J. and Wiemer, S.: Estimating ETAS:

457   The effects of truncation, missing data, and model assumptions, J. Geophys. Res.

458   Solid Earth, 121, 449-469, doi: 10.1002/2016JB012809, 2017.

459   Shapiro, S. A. and Dinske, C.: Scaling of seismicity induced by nonlinear fluid-rock

460   interaction, J. Geophys. Res., 114, B09307, doi: 10.1029/2008JB006145, 2009.

461   Shaw, B. E. and Scholz, C. H.: Slip-length scaling in large earthquakes: Observations

462   and theory and implications for earthquake physics, Geophys. Res. Lett., 28, 2995-

463   2998, 2001.

464   Shearer, P. M.: Space-time clustering of seismicity in California and the distance

465   dependence of earthquake triggering, J. Geophys. Res., 117, B10306, doi:

466   10.1029/2012JB009471, 2012.

467   Toda, S., Stein, R. S., Richards-Dinger, K. and Bozkurt, S.: Forecasting the evolution

468   of seismicity in southern California: Animations built on earthquake stress transfer,

469   J. Geophys. Res., 110, B05S16, doi: 10.1029/2004JB003415, 2005.

470   Tormann, T., Wiemer, S. and Mignan, A.: Systematic survey of high-resolution b

471   value imaging along Californian faults: inference on asperities, J. Geophys. Res.

472   Solid Earth, 119, 2029-2054, doi: 10.1002/2013JB010867, 2014.

473   Utsu, T.: Aftershocks and Earthquake Statistics (1): Some Parameters Which

474   Characterize an Aftershock Sequence and Their Interrelations, J. Faculty Sci.

475   Hokkaido Univ. Series 7 Geophysics, 3, 129-195, 1970a.

476   Utsu, T.: Aftershocks and Earthquake Statistics (2): Further Investigation of

477   Aftershocks and Other Earthquake Sequences Based on a New Classification of

478   Earthquake Sequences, J. Faculty Sci. Hokkaido Univ. Series 7 Geophysics, 3,

479   197-266, 1970b.

480   Utsu, T., Ogata,, Y. and Matsu'ura, R. S.: The Centenary of the Omori Formula for a

481   Decay Law of Aftershock Activity, J. Phys. Earth, 43, 1-33, 1995.

482   van der Elst, N. J. and Shaw, B. E.: Larger aftershocks happen farther away:

483   Nonseparability of magnitude and spatial distributions of aftershocks, Geophys.

484   Res. Lett., 42, 5771-5778, doi: 10.1002/2015GL064734, 2015.

485   Varnes, D. J.: Predicting Earthquakes by Analyzing Accelerating Precursory Seismic

486   Activity, Pure Appl. Geophys., 130, 661-686, 1989.

487   Yamanaka, Y. and Shimazaki, K.: Scaling Relationship between the Number of

488   Aftershocks and the Size of the Main Shock, J. Phys. Earth, 38, 305-324, 1990.

489   Zaliapin, I., Gabrielov, A., Keilis-Borok, V. and Wong, H.: Clustering Analysis of

490   Seismicity and Aftershock Identification, Phys. Rev. Lett., 101, 018501, doi:

491   10.1103/PhysRevLett.101.018501, 2008.

492   Zaliapin, I. and Ben-Zion, Y.: Earthquake clusters in southern California I:

493   Identification and stability, J. Geophys. Res. Solid Earth, 118, 2847-2864, doi:

494   10.1002/jgrb.50179, 2013.

495

496   **Figures**
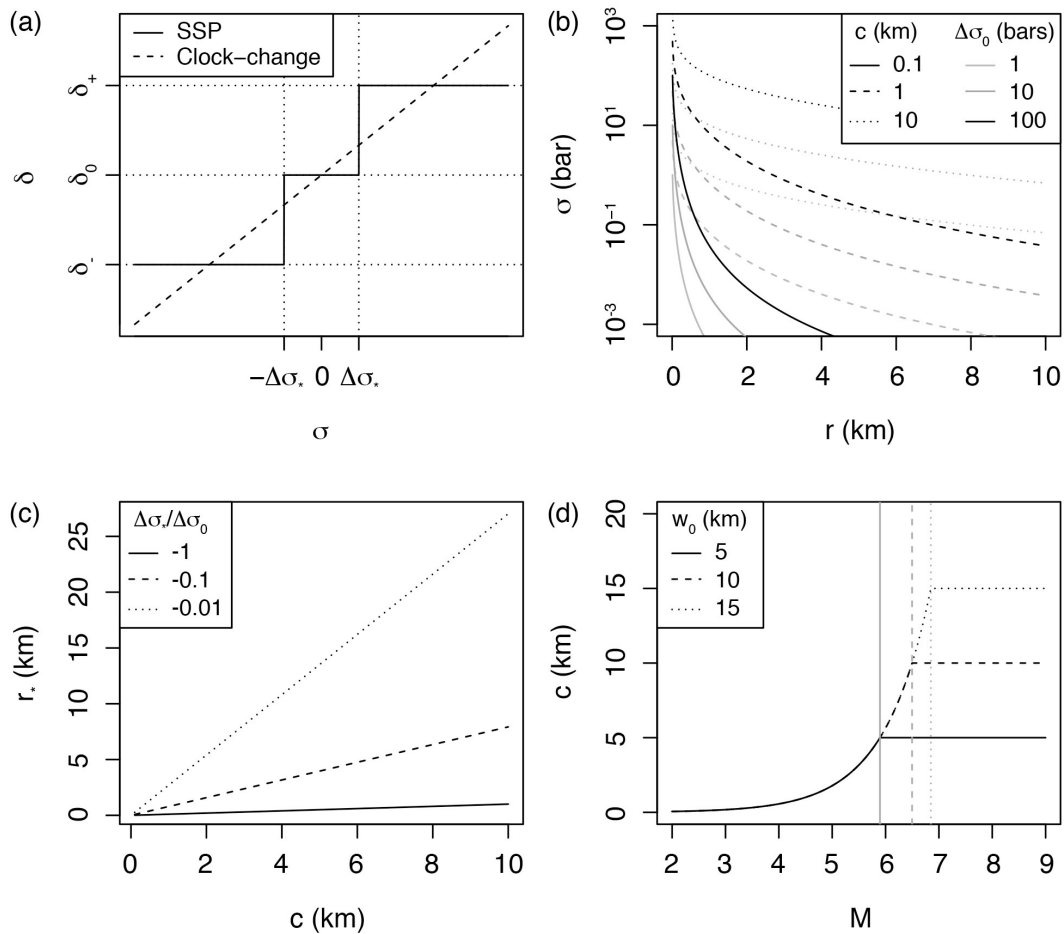
497

498   **Figure 1.** Definition of the aftershock solid envelope in a permanent static stress field:

499   (a) Event density stress step-function $\delta(\sigma)$ (Eq. 5) of the Solid Seismicity Postulate

500   (SSP) in comparison to the linear clock-change model; (b) Static stress σ versus

501   distance r for different effective crack radii c and rupture stress drops $\Delta\sigma_0$ (Eq. 6); (c)

502   Linear relationship between effective crack radius c and aftershock solid envelope

503 radius r_* for different $\Delta\sigma_*/\Delta\sigma_0$ ratios (Eq. 7); (d) Relationship between mainshock

504 magnitude M and effective crack radius c for different seismogenic widths w_0 (Eq. 8).

505
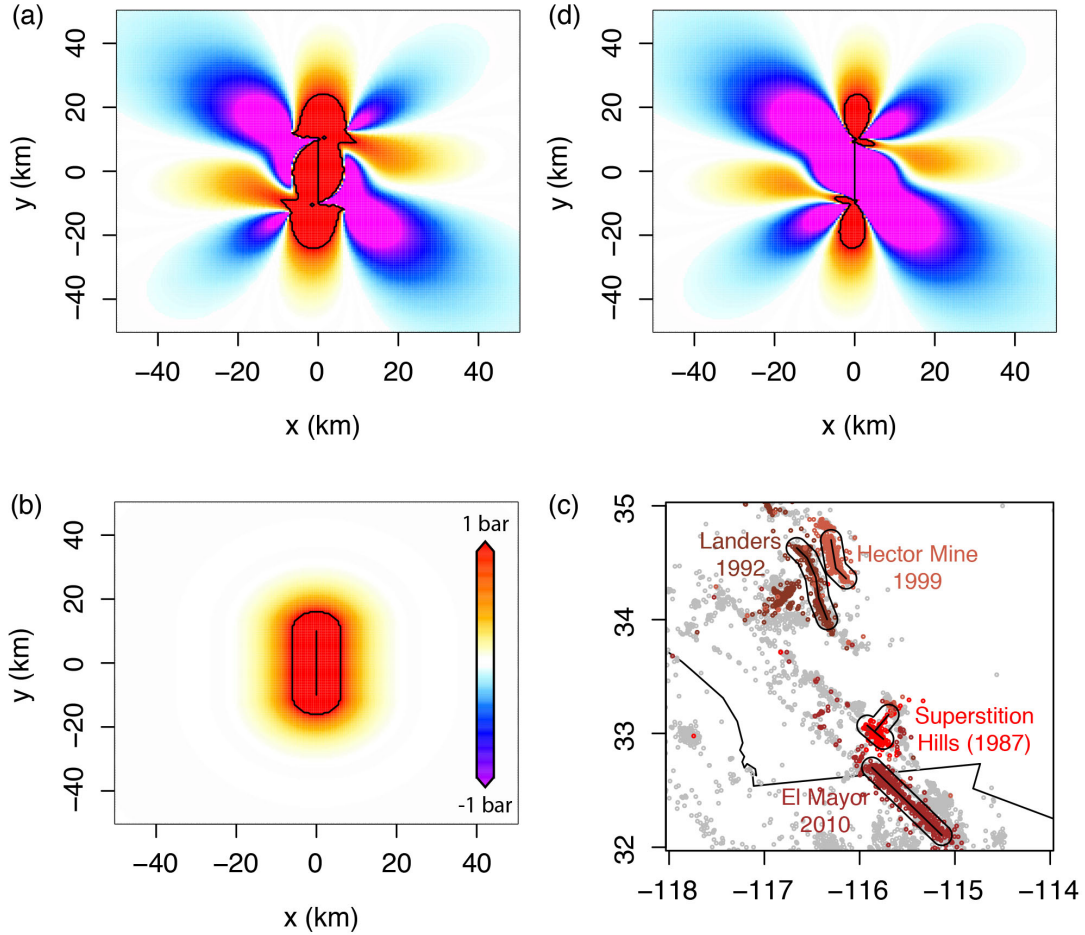
506

507 **Figure 2.** Possible static stress fields and inferred aftershock spatial distribution: (a)

508 Right-lateral Coulomb stress field for optimally oriented faults, where the mainshock

509 relieves all of the regional stresses $\sigma_r = 10$ bar, with $\Delta\sigma_0 \approx -Gs/L \approx$ - 10 bar ($G =$

510 $3.3.10^5$ bar the shear modulus, $s = 0.6$ m the slip, $L = 20$ km the fault length, and $w =$

511 10 km the fault width); (b) Radial static stress field computed from Eq. (6) with $\Delta\sigma_0 =$

512 -10 bar and $c = \sqrt{(Lw)/\pi}$ for consistency with (a); (c) Aftershock distribution of the

513 largest strike-slip events in the Southern California relocated catalog, identified here

514 as all events occurring within one day of the mainshock (see Data section 3.1); (d)

515   Right-lateral Coulomb stress field for optimally oriented faults, where the mainshock

516   relieves only a fraction of the regional stresses σ_r = 100 bar with $\Delta\sigma_0$ = -10 bar (same

517   rupture as in (a)) – The black contour represents 1 bar in (a), (b) and (d), and a 10 km

518   distance from rupture in (c). Coulomb stress fields of (a) and (d) were computed using

519   the Coulomb 3 software (Lin and Stein, 2004; Toda et al., 2005).

520
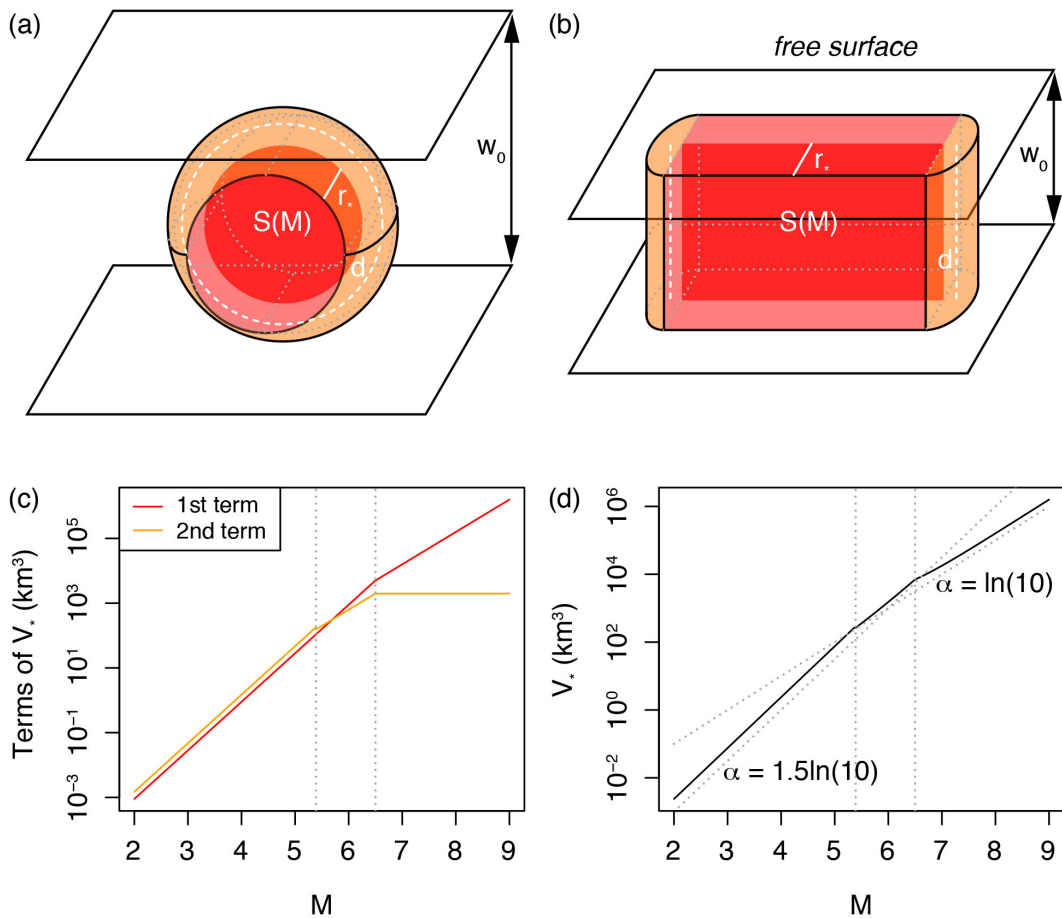
521

522   **Figure 3.** Geometric origin of the aftershock productivity law: (a) Sketch of the

523   aftershock solid for a small mainshock rupture represented by a disk; (b) Sketch of the

524   aftershock solid for a large mainshock rupture represented by a rectangle; (c) Relative

525   role of the two terms of Eq. (9), here with w_0 = 10 km and $\frac{\Delta\sigma_*}{\Delta\sigma_0}$ = -0.1 (to first estimate

526   c and r_* from Eqs. 8 and 7, respectively); (d) Aftershock productivity law (normalized

527   by δ_+) predicted by Solid Seismicity (Eq. 11). This relationship is of the same form as

528   the Utsu productivity law (Eq. 1) for large *M* (see text for an explanation of the lack

529   of break in scaling in Eq. 1 for small *M*). Dotted vertical lines represent *M* for

530      $c(M) + r_*(M) = \frac{w_0}{2}$ and $S(M) = \pi w_0^2$, respectively.

531

532
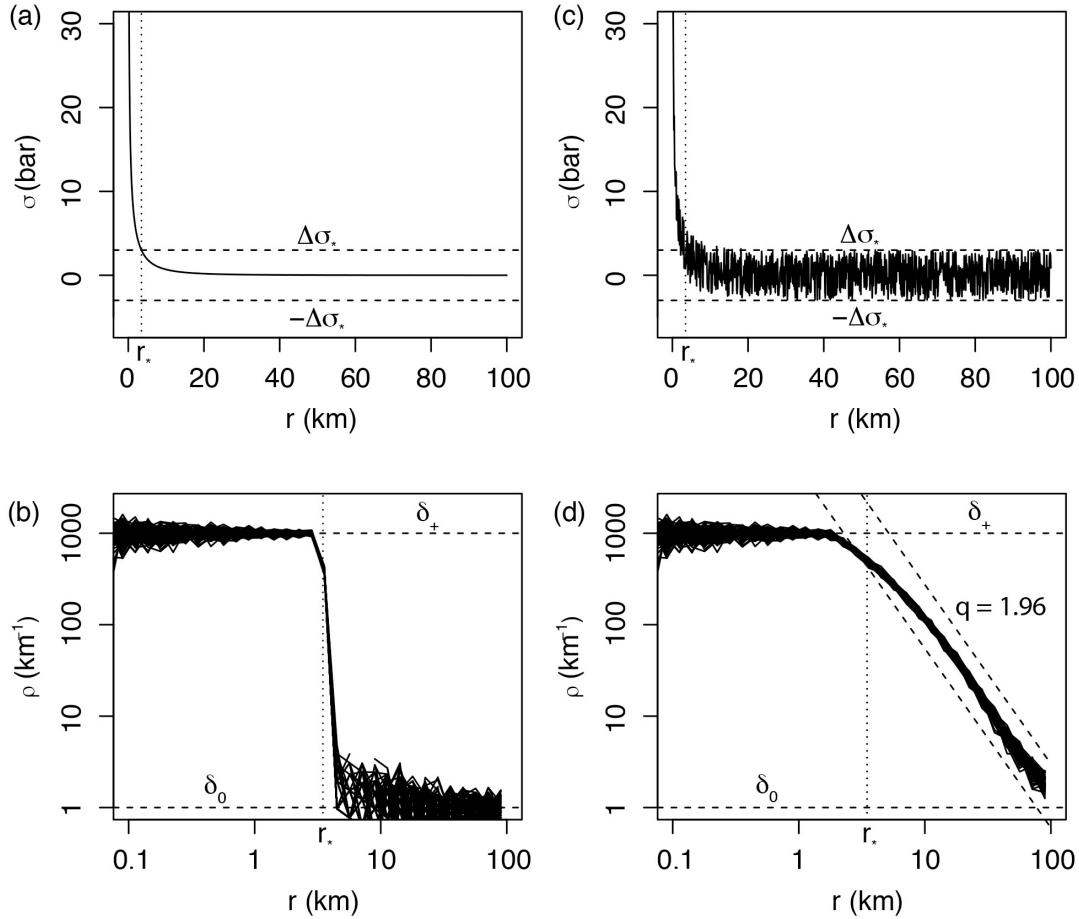
Figure 4. Spatial distribution of aftershocks following the SSP. (a) Smooth static

stress field as a function of distance *r* from the mainshock, with $\Delta\sigma_0 = -10$ bar and $c =$

10 km (Eq. 6); (b) Step-like aftershock spatial linear density $\rho(r)$ with $\delta_+ = 1000$

events per km, $\delta_0 = 1$ event per km and $\Delta\sigma_* = -0.3\Delta\sigma_0$ (*ad-hoc* ratio yielding $r_* = 3.5$

km; Eq. (7) – event distances sampled from the $\delta(r)$ distribution, repeated 100 times).

Such distribution is not observed in Nature; (c) Same as (a) but with random uniform

noise representative of spatial heterogeneities added to the regional stress field; (d)

540 Power-law-like aftershock spatial linear density ρ(r) with power exponent MLE

541 estimate $q = 1.96$, representative of real aftershock observations (see Fig. 5a), due to

542 the addition of uniform noise to the static stress field.

543
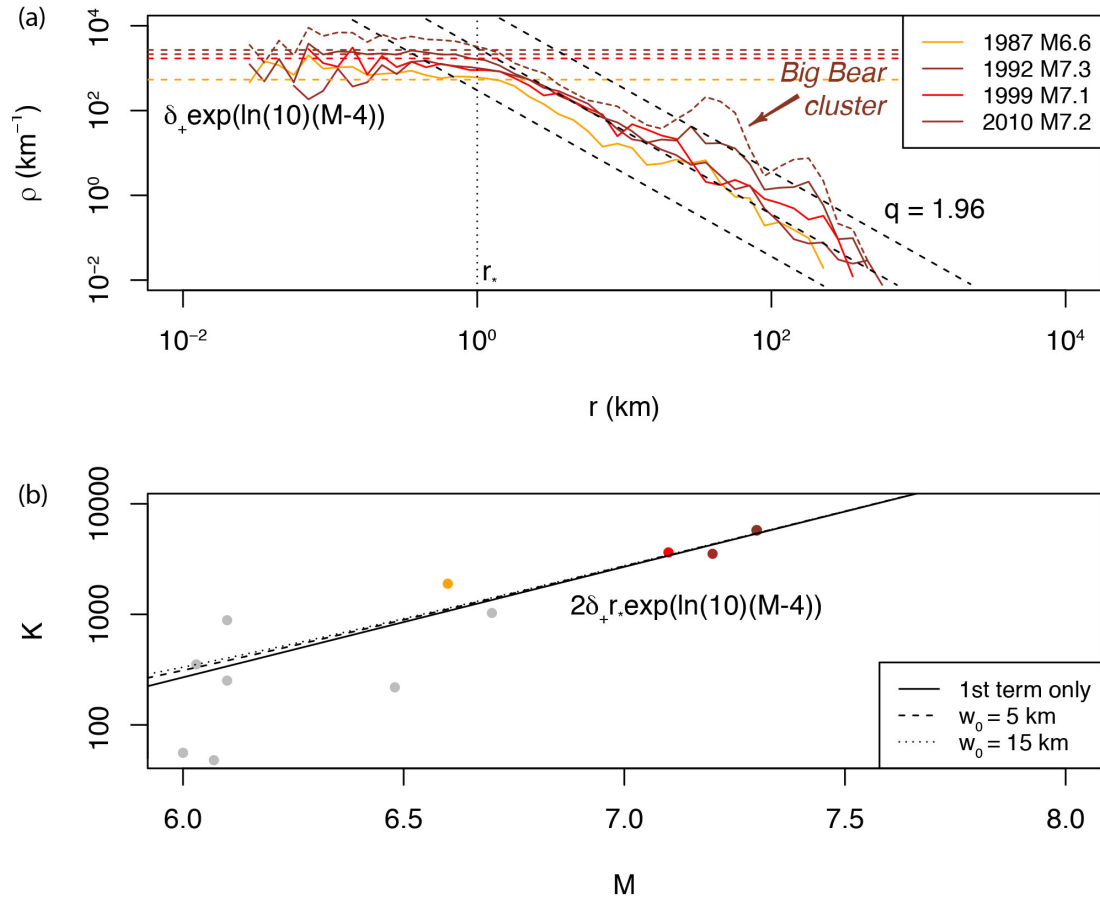
544

545 **Figure 5.** Estimating the Solid Seismicity parameters from the spatial distribution of

546 aftershocks: (a) Spatial linear density distribution ρ(r) of aftershocks for the four

547 largest strike-slip mainshocks in Southern California (with first-generation

548 aftershocks only; the density distribution comprising all aftershocks generated by the

549 Landers mainshock is represented by the dotted curve to illustrate the type of spatial

550 heterogeneity, such as the Big Bear cluster, not considered in the present study – see

551 also Fig. 2c). The Solid Seismicity parameters $r_* = 1$ km and $\delta_+(m_0 = 2) = 1.23$

552 events/km^3 can be retrieved from the observed plateau ρ($r < r_*$), in agreement with the

553 SSP (see Fig. 4d). Note that the spatial power-law decay at high r is similar to the one

554 expected by the SSP in the case of a static stress field with additive uniform noise

555 (expected $q = 1.96$ represented by the dashed black lines); (b) Aftershock productivity

556 K for $M > 6$. The curves represent the productivity law as defined by Solid Seismicity

557 (Eq. 17) for different w_0 values (first term only corresponds to $w_0 = 0$; Eq. 18).

558
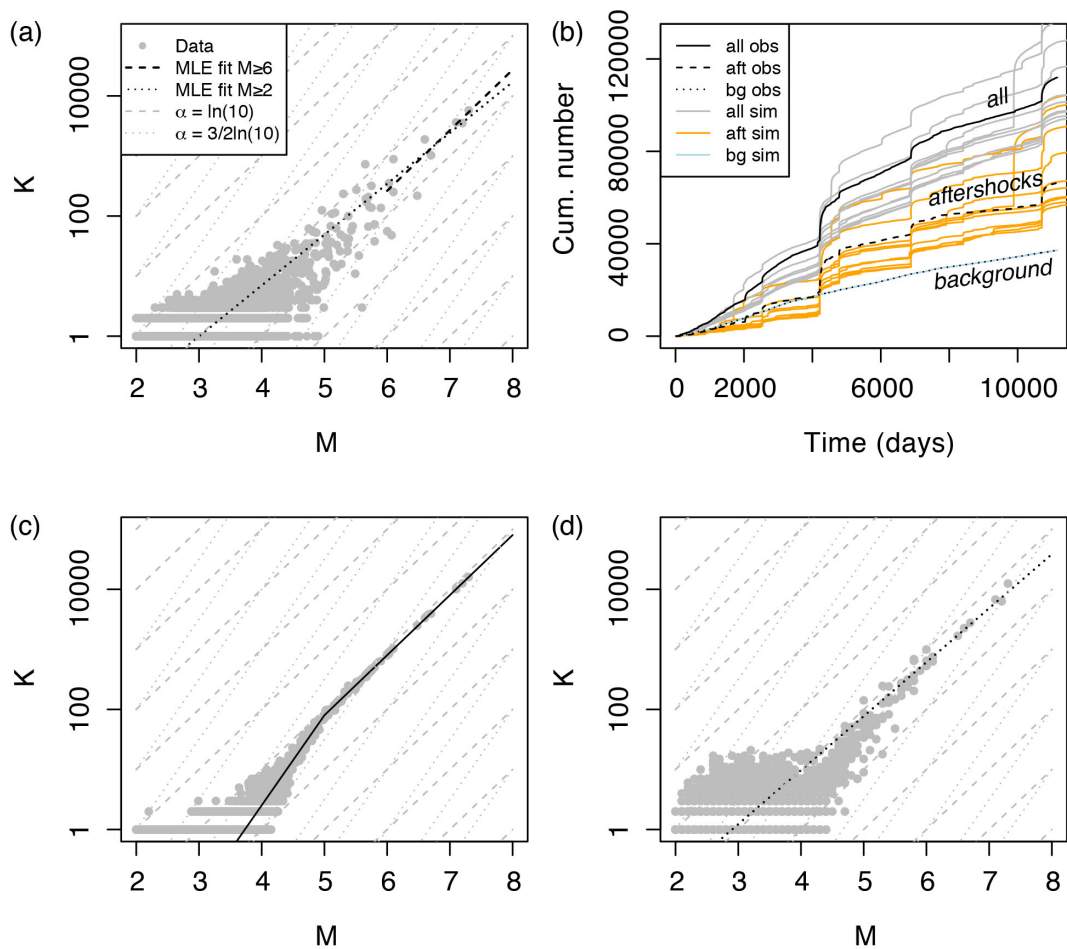
559

560 **Figure 6.** Aftershock productivity defined as the number of aftershocks $K(m_0 = 2)$ per

561 mainshock of magnitude M: (a) Observed aftershock productivity in Southern

562 California with aftershocks selected using the nearest-neighbor method; (b)

563 Seismicity time series with distinction made between background events and

564 aftershocks, observed ("obs", in black) and ETAS-simulated ("sim", colored); (c)

565 True simulated aftershock productivity with kink, defined from Eq. (20); (d)

566 Retrieved simulated aftershock productivity with aftershocks selected using the

567 nearest-neighbor method - Data points in (a), (c) and (d) are represented by grey dots;

568 the model MLE fits are represented by the dashed and dotted black lines for $M \geq 6$

569 and $M \geq m_0$, respectively; dashed and dotted grey lines are visual guides to $\alpha =$

570 $3/2\ln(10)$ and $\ln(10)$, respectively.

571